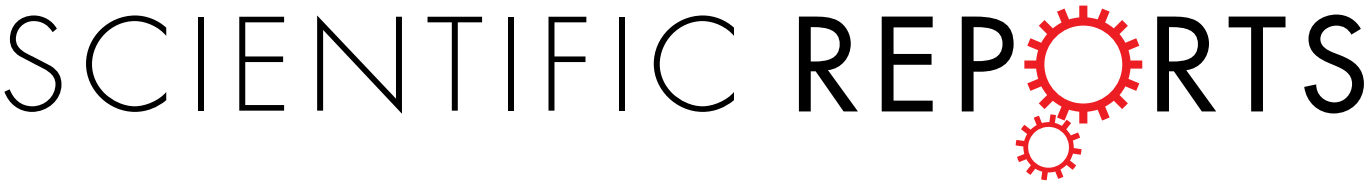

OPEN

UV and visible light photocatalytic activity of Au/TiO_2 nanoforests with Anatase/Rutile phase junctions and controlled Au locations

Received: 03 June 2016
Accepted: 19 December 2016
Published: 24 January 2017

Yang Yu[1], Wei Wen[2], Xin-Yue Qian[1], Jia-Bin Liu[1] & Jin-Ming Wu[1]

To magnify anatase/rutile phase junction effects through appropriate Au decorations, a facile solution-based approach was developed to synthesize Au/TiO_2 nanoforests with controlled Au locations. The nanoforests cons®isted of anatase nanowires surrounded by radially grown rutile branches, on which Au nanoparticles were deposited with preferred locations controlled by simply altering the order of the fabrication step. The Au-decoration increased the photocatalytic activity under the illumination of either UV or visible light, because of the beneficial effects of either electron trapping or localized surface plasmon resonance (LSPR). Gold nanoparticles located preferably at the interface of anatase/rutile led to a further enhanced photocatalytic activity. The appropriate distributions of Au nanoparticles magnify the beneficial effects arising from the anatase/rutile phase junctions when illuminated by UV light. Under the visible light illumination, the LSPR effect followed by the consecutive electron transfer explains the enhanced photocatalysis. This study provides a facile route to control locations of gold nanoparticles in one-dimensional nanostructured arrays of multiple-phases semiconductors for achieving a further increased photocatalytic activity.

Semiconductor photocatalysis utilizes natural sun light or artificial light sources to initiate catalytically specific redox reactions under mild conditions, which finds wide applications in environmental remediation, photocatalytic water-splitting, and CO_2 reduction[1]. The emergence of novel photocatalysts[2–5] in recent years does not hinder researchers' enthusiasm on titanium dioxide (TiO_2), which is one of the most traditional yet promising semiconductors for photocatalytic applications because of its exceptional merits of biological friendliness, chemical inertness, low cost, and earth-abundance[1]. The high charge recombination rate and the wide band gap (3.0–3.2 eV) impose a fundamental restriction on the overall photocatalytic efficiency for TiO_2[1], which are the focus of numerous studies ever since Fujishima and Honda's pioneer work on TiO_2 photocatalysis[6].

Decorating TiO_2 with noble metal nanoparticles such as Pt[7], Ag[8], Pd[9], and Au[10–13] is an effective tactic to improve the photocatalytic activity. The noble metal nanoparticles contact closely with TiO_2 to form Schottky barriers, which drive photogenerated electrons from the n-type TiO_2 to the noble metals and enhance the charge separation rate and the photocatalytic activity. For TiO_2 decorated with Au and Ag, there is an additional effect, the localized surface plasmon resonance (LSPR), which contributes to a strong absorption of the visible light and thus the photocatalytic performance under the visible light illumination[13–15]. The LSPR effect is affected readily by shape[16], size[17–19], and content[20] of Au nanoparticles, as well as characteristics of the TiO_2 supports[13,18,21,22].

Energy band engineering is another interesting topic for improving photocatalytic activity of TiO_2[23]. The anatase/rutile phase junction has been argued to favor the charge separation of TiO_2[24–26]. Compositing TiO_2 with other semiconductors possessing either a wider or a narrower band gap also results in efficient charge separations and/or enhanced light harvesting from the solar light[27–29]. Not surprisingly, such TiO_2-based composite semiconductors or TiO_2 with mixed phases could be decorated with noble metals to further enhance the photocatalytic performance[13,14,22]. Recently, the importance of the architecture of Au/TiO_2 nanoparticles has been noted under the visible light illumination[13,14].

[1]State Key Laboratory of Silicon Materials and School of Materials Science and Engineering, Zhejiang University, Hangzhou 310027, P. R. China. [2]College of Mechanical and Electrical Engineering, Hainan University, Haikou, 570228, P. R. China. Correspondence and requests for materials should be addressed to J.-M.W. (email: msewjm@zju.edu.cn)

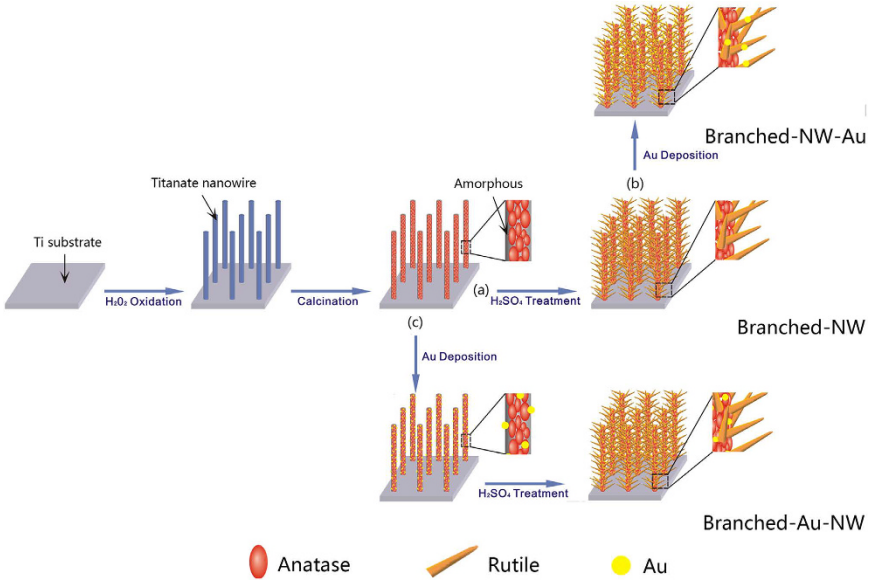

Figure 1. A schematic diagram showing the formation of the branched TiO_2 nanowires (**a**, Branched-NW), those after the Au-loading (**b**, Branched-NW-Au), and the branched TiO_2 nanowires with an intermediate Au-loading (**c**, Branched-Au-NW).

When compared with nanoparticles, one-dimensional (1D) semiconducting nanostructures such as nanorods and nanowires have been found to enhance the photocatalytic activity of TiO_2 with distinct charge transport capabilities[30,31]. Imposing branches on the surface of well-aligned 1D nanostructures to form branched nanowire arrays, also termed as nanotrees or nanoforests, further increases the performance because of the enhanced active sites and light harvesting capability[31–34]. In practical photocatalysis for wastewater treatments, TiO_2 thin films avoid the nuisance powder recovering procedure. It is thus of great importance to develop TiO_2 thin films with high photocatalytic activity. Based on the literature, it can be anticipated that decorating noble metals on controlled locations in TiO_2 nanoforests could achieve enhanced photoelectrochemical performances.

In this work, an architectural design was implemented to study the possible effects of the location of Au nanoparticles decorated on TiO_2 nanoforests with anatase/rutile phase junctions. Simply altering the order of the fabrication step (Fig. 1), Au nanoparticles were located preferably either on the interface of anatase/rutile phase junctions, or on rutile branches, which in turn affected readily the photocatalytic efficiency towards photodegradations of rhodamine B in water under the illumination of either UV or visible light. Efforts were made to clarify the possible mechanisms that cause the distinct photocatalytic activity.

Results and Discussions

Morphology and phase characterizations. Supplementary Figure S1 shows FESEM images of the TiO_2 nanoforests and those after Au-loading at various locations. It can be seen that quasi-aligned 1D branched nanowires covered homogeneously the Ti substrates. The Au-loading procedures induced no significant change in morphologies. Figure 2 illustrates FESEM, TEM, HRTEM, selected area electron diffraction (SAED), and EDS analysis results of the Branched-Au-NW (refer to Fig. 1 for the sample ID). The thickness of the TiO_2 nanoforests is ca. 1 μm. An intermediate layer ca. 1 μm in thickness, which consisted of compact nanoparticles, can also be seen between the top layer and the substrate (Fig. 2a–c).

The low-magnification TEM image shows clearly a typical branched nanowire that is decorated with Au nanoparticles (Fig. 2e). The average diameter of the nanorod branch is ca. 10 nm and the length is ca. 45 nm; while the Au particles have an approximately spherical shape that is 8–9 nm in diameter. The HRTEM image (Fig. 2d) exhibited that the backbone is formed by many tiny crystal grains with a lattice spacing of ca. 0.35 nm, which can be attributed to the (101) facet of anatase TiO_2. The fringe with inter-plane spaces of ca. 0.32 nm on the branch can be discerned, which is attributed to the (110) crystal plane of rutile TiO_2. Locating between the anatase backbone and the rutile branch, fringes with inter-plane spaces of ca. 0.235 nm can be seen clearly, which can be assigned to the (111) facet of Au. Hence, the HRTEM observations suggest that, for the Branched-Au-NW specimen, the well-crystalized single-crystalline rutile nanorods grew along the polycrystalline anatase TiO_2 nanowires with an arbitrary angular orientation; whilst most Au nanoparticles located at the interface between the backbone and the branch, which contacted closely with both anatase and rutile. Figure 2f demonstrates the SAED pattern of the branched nanowire shown in Fig. 2e. Multi-rings characteristic of a mixture of anatase and rutile can be discerned, which is in good accordance with the HRTEM observations (Fig. 2d). The EDS mapping (Fig. 2g) suggests the homogenous distributions of Ti, O, N, and S throughout the Branched-Au-NW. A spot corresponding to an Au nanoparticle located between the anatase trunk and rutile branch can be discerned.

The crystal structure of the TiO_2 nanoforests can find support from both XRD patterns and Raman spectra. XRD peaks corresponding to both anatase and rutile can be discerned, besides those arising from the metallic

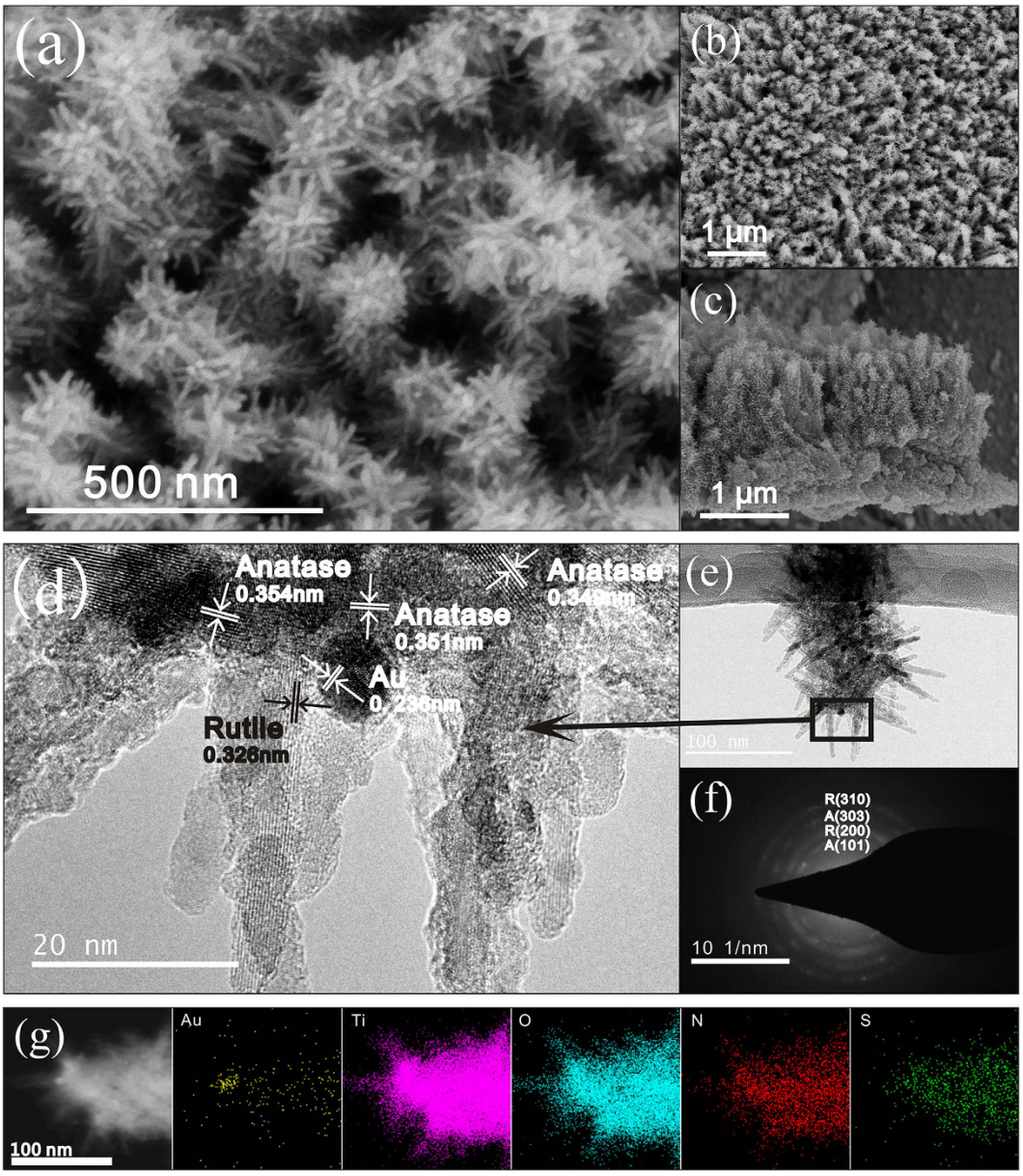

Figure 2. (**a**) High and (**b**) low magnification top view, (**c**) cross-sectional FESEM images of the Branched-Au-NW; (**d**) HRTEM, (**e**) low-magnification TEM, and (**f**) the corresponding SAED of the Branched-Au-NW; (**g**) TEM image of another Branched-Au-NW and the corresponding EDS mapping images of Au, Ti, O, N and S.

Ti substrates (Fig. 3a). It is not surprising that three specimens exhibited similar XRD patterns, indicating that the phase structure of TiO_2 does not change after the deposition of gold nanoparticles. Trace srilankite TiO_2 can also be discerned. The corresponding Raman spectrum suggests more clearly the coexistence of anatase, rutile, and srilankite (Fig. 3b). Both XRD (Fig. 3a) and SAED patterns (Fig. 2f) exhibit no signals corresponding to Au, which can be contributed to the minor amounts of Au nanoparticles. It is noted that only one peak appeared in both XRD patterns and Raman spectra, which is a weak proof of the existence of srilankite TiO_2. However, a previous study[35] revealed that, the srilankite TiO_2 was detected on a low temperature derived TiO_2 thin film. In that case, Raman peaks were identified at 168, 314, 354 and 425 cm^{-1}, which have been contributed to srilankite TiO_2. Also, the XRD peak located at ca. 31.5° was identified. Therefore, we believe it is safe to ascribe the present XRD peak located at ca. 31.5° (Fig. 3a) and the Raman peak located at ca. 314 cm^{-1} (Fig. 3b) to srilankite TiO_2.

Au contents. The atomic ratio of Au/Ti was measured by ICP-MS to be 0.36% and 0.51%, for the specimens of Branched-Au-NW and Branched-NW-Au, respectively. By using the defined Au-loading parameters (identical $HAuCl_4$ solution and photo- reduction time), the Branched-Au-NW contained less Au nanoparticles when compared with the Branched-NW-Au. This may be contributed to the different phase compositions of the TiO_2 films before Au-decorations. For the Branched-Au-NW, Au-loading was performed on poorly crystallized anatase TiO_2 nanowires; whilst for the Branched-NW-Au, Au-loading was conducted on TiO_2 nanoforests consisted of rutile

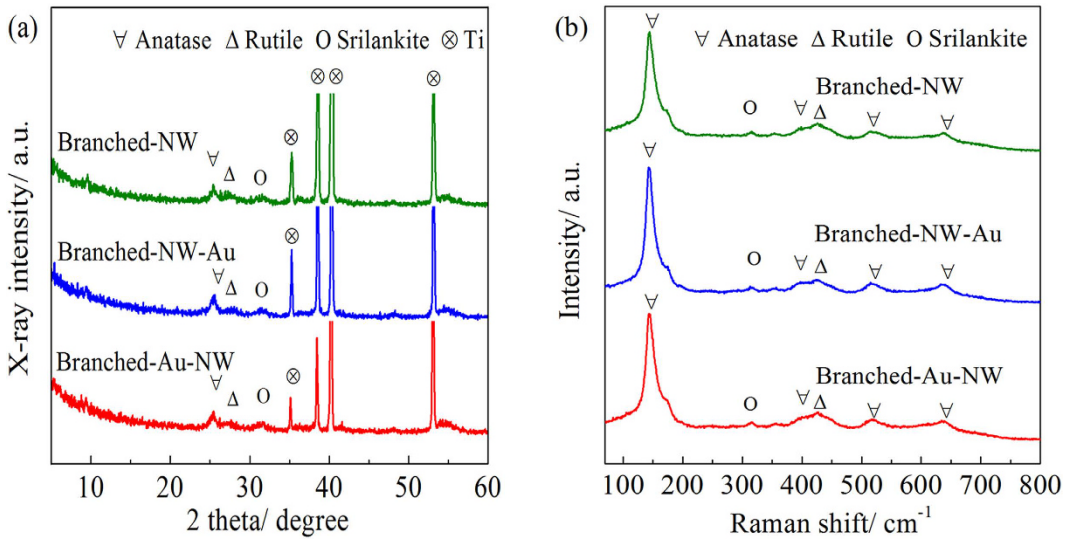

Figure 3. (**a**) XRD patterns and (**b**) Raman spectra of the Branched-NW, Branched-NW-Au, and Branched-Au-NW.

TiO_2 branches that grow radially around the poorly crystallized anatase TiO_2 trunk[34]. It is well established that the anatase/rutile phase junctions facilitate charge separations[24–26] and hence the photocatalytic efficiency for the Au-loading, which explained the higher content of gold nanoparticles decorated on Branched-NW-Au. It is also argued that Au nanoparticles form more easily on the rutile surface because a number of oxygen vacancies act as the crystal nucleation sites[13].

The surface compositions of the Branched-Au-NW were analyzed by XPS. Figure 4a shows that the surface layer of the Branched-Au-NW is composed of Ti, O, Au, N, and S, which is consistent to the EDS mapping images (Fig. 2g). The XPS spectrum of Ti 2p exhibits two dominant peaks, which correspond to Ti $2p_{1/2}$ at 464.6 eV and Ti $2p_{3/2}$ at 458.8 eV, indicating that Ti exist in the form of Ti^{4+}. The separation between the two peaks is 5.8 eV (Fig. 4b), which is in agreement with the XPS data in the literature[7]. As shown in Fig. 4c, the O 1 s spectrum can be fitted by two components: a higher binding energy (BE) peak near the 531.7 eV, originating from the hydroxyl group (-OH)[36], and a lower BE, in the vicinity of 530.1 eV, originating from the crystal lattice oxygen (Ti–O–Ti).

The XPS spectrum of Au can be separated to two peaks, with a lower BE at 83.4 eV and a high BE at 87.1 eV, corresponding to Au $4f_{7/2}$ and Au $4f_{5/2}$, respectively (Fig. 4d). The typical Au $4f_{7/2}$ peak locates at 84.0 eV[37] for bulk metallic gold; the slight shift in BE to a lower value can be ascribed to the redistribution of the electrons at the Au-TiO_2 contact interfaces, because of the difference in the work function between Au (5.27 eV) and TiO_2 (4.1 eV). This is an indication that Au nanoparticles interact with the adjacent TiO_2[14,37,38]. The electron transferring from TiO_2 to Au nanoparticles is therefore facilitated, which increases the valence charge density of Au atoms and reduces the binding energy of Au in the TiO_2 film.

The binding energy of N 1 s locates at ca. 399.8 eV, which can be assigned to nitrogen species bonding to various surface oxygen sites N-O, or N-N, and N-C bonds (Fig. 4e)[39]. The incorporation of N into the Branched-Au-NW film is believed to result from the decomposition of melamine during the fabrication of the titanate nanowires. After the H_2SO_4 treatment, sulfate ions also incorporate into the TiO_2 film, which gave the XPS peak at 168.9 eV (Fig. 4f)[36].

Table 1 lists the surface compositions of the two Au-decorated TiO_2 nanoforests derived by the XPS analysis. The atomic Au/Ti ratio determined by the XPS analysis is ca. 0.27% for Branched-Au-NW, which is lower than that of Branched-NW-Au. The atomic Au/Ti ratios evaluated by XPS roughly agreed with that derived by the ICP-MS measurement.

Growth of the TiO_2 Nanoforests with Controlled Au-location. Figure 5a,b shows that, Au nanoparticles were intimately decorated on the surface of the poorly crystallized anatase TiO_2 nanowires before the final H_2SO_4 treatment. That is to say, in the current tactic to synthesize Branched-Au-NW, Au nanoparticles were firstly deposited on the surface of the nanowires which were just subjected to the intermediate calcination. During the final H_2SO_4 treatment, the poorly crystallized anatase TiO_2 nanowires were partly attacked by H_2SO_4, which released hydrated Ti(IV) ions into the acid solution[34]. Once the Ti(IV) ions accumulated to a critical concentration, nucleation and subsequent growth of rutile TiO_2 branches around the anatase TiO_2 trunk occurred. It seems that the edges formed between the nanowires and the decorated Au nanoparticles provide heterogeneous nucleation sites for the TiO_2 branches, which resulted in the preferred locations of the Au nanoparticles around the junctions of the anatase trunk and rutile branch.

When the Au-decoration procedure was moved to be the final step, the Au nanoparticles did not locate preferably on the anatase/rutile phase junctions any more. Because of certain "tip" effects, most of Au nanoparticles located on the surface of the rutile branch (Fig. 5c,d), rather than on the interface of rutile branch and anatase backbone. In addition, for the Branched-NW film, because the anatase trunk is surrounded by rutile branches,

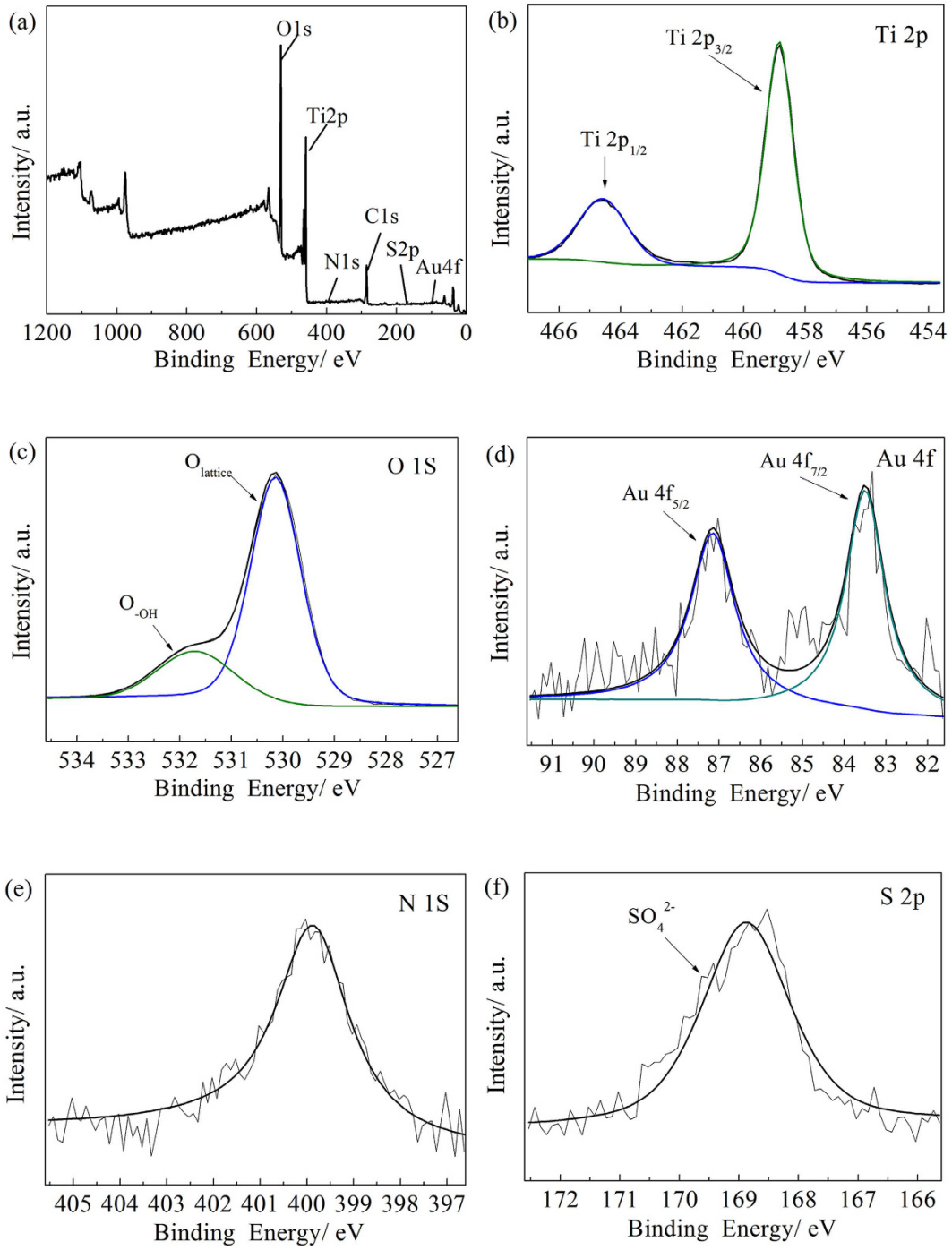

Figure 4. (**a**) Wide scan and high-resolution XPS spectra of (**b**) Ti 2p, (**c**) O 1 s, (**d**) Au 4 f, (**e**) N 1 s, and (**f**) S 2p for the Branched-Au-NW.

	C	N	S	O	Au	Ti	Au/Ti by XPS	Au/Ti by ICP
Branched-NW-Au	13.71	0.88	0.56	56.30	0.14	28.41	0.49%	0.51%
Branched-Au-NW	25.71	0.97	1.10	49.70	0.06	22.46	0.27%	0.36%

Table 1. Surface compositions (in at. %) of Au-decorated TiO_2 nanoforests obtained by XPS.

Au nanoparticles had a higher possibility to sit on rutile. Therefore, simply altering the Au-loading order fulfilled the control in the location of Au nanoparticles, which affects readily the resultant photocatalytic performance of the Au-decorated TiO_2 nanoforests, as will be discussed later.

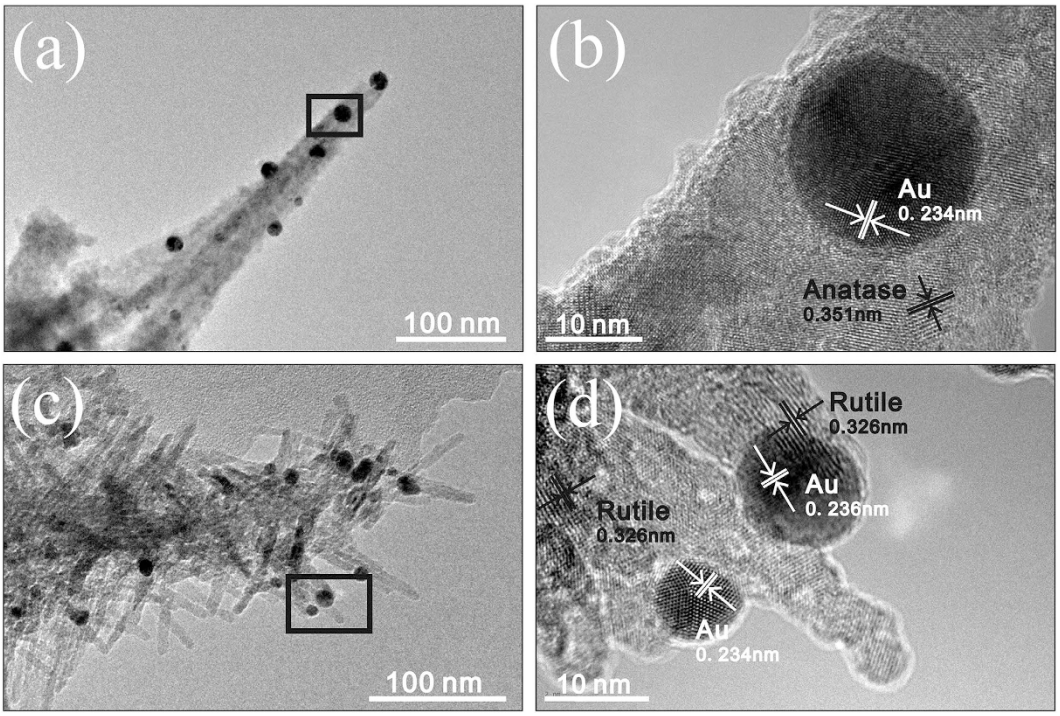

Figure 5. (**a**,**b**) TEM and HRTEM images of the Au-decorated nanowires just before the final H_2SO_4 treatment; (**c**,**d**) TEM and HRTEM images of the Branched-NW-Au.

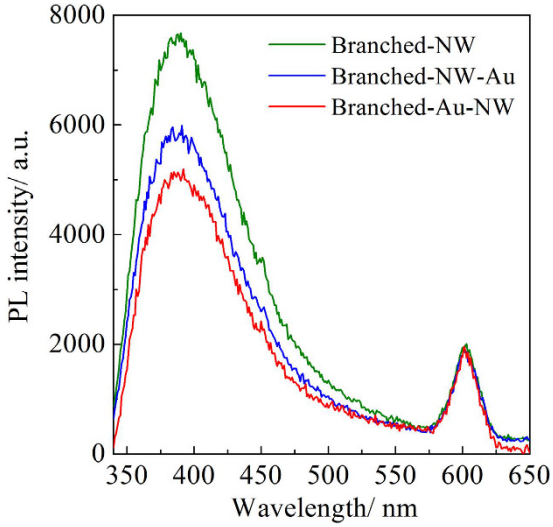

Figure 6. Ambient PL spectra of the Branched-NW, Branched-NW-Au, and Branched-Au-NW.

PL and UV-Vis DRS Characterizations. Figure 6 shows the PL spectra of the three specimens, all of which possessed a feature that consists of two emission peaks in the UV-visible range. The UV emission centered at 400 nm is related to the electron transition from the valence band and the conduction band[38], and the emission centered at around 608 nm may arise from the recombination of photo-generated holes with the electrons in singly occupied oxygen vacancies[40]. It can be seen that, the intensity of UV emission decreased in the order of Branched-NW, Branched-NW-Au, and Branched-Au-NW. Therefore, the Au-decoration suppresses the charge recombination, which is closely related to the location of Au nanoparticles.

Figure 7a illustrates the UV-Vis diffuse reflectance spectra collected from the three specimens. The Branched-Au-NW film exhibited the lowest reflectance over the visible light region, which suggests the highest visible light harvesting capability when compared with the Branched-NW and the Branched-NW-Au. The increasing absorption can be ascribed to the LSPR effect arising from Au nanoparticles. A strong oscillation of the metal's surface free electrons with the varying electric field of the incident light absorbs the energy of photon

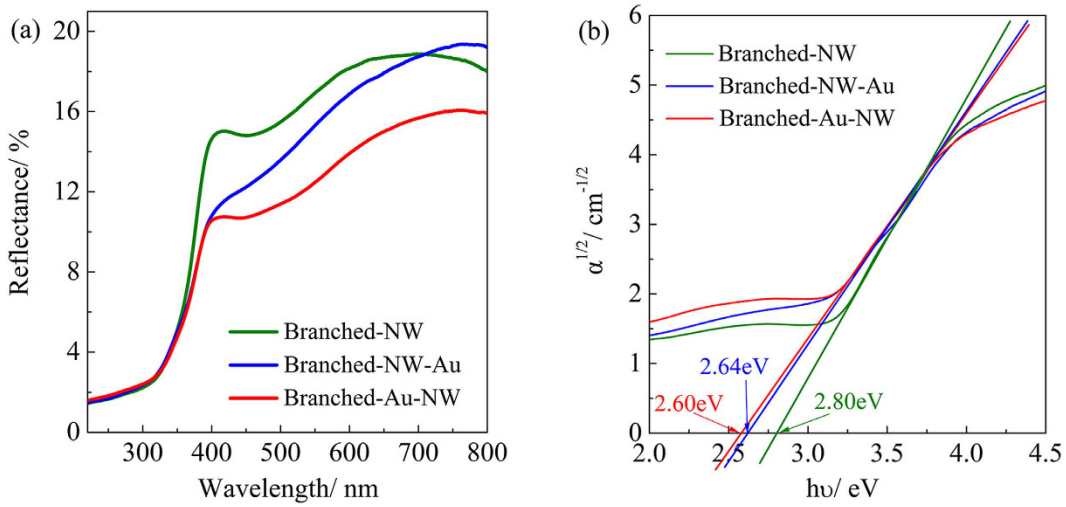

Figure 7. (**a**) UV-Vis diffuse reflectance spectra of the Branched-NW, Branched-NW-Au, and Branched-Au-NW; (**b**) the spectra in an $\alpha^{1/2}$~$h\nu$ coordinate to evaluate the band gap.

and conveys to electrons to form surface plasmons, which decay to hot electron-hole pairs; as a result, the light response of the Au-decorated specimens in the visible light region is enhanced[41,42].

Assuming an indirect transition between band gaps, the band gaps of TiO_2 can be estimated by extrapolating the tangent line in the plot of $\alpha^{1/2}$ against $h\upsilon$[43], where α is the absorption coefficient and the $h\upsilon$ is the photon energy. Figure 7b demonstrates that the Branched-Au-NW possessed an indirect band gap of 2.61 eV, which is lower than the value of 2.64 eV and 2.80 eV determined for the Branched-NW-Au and Branched-NW, respectively. The relatively lower band gap of 2.80 eV for Branched-NW, when compared with bulk TiO_2 (3.2 eV for anatase and 3.0 eV for rutile), can be contributed to the N-doping (Fig. 4e) and the significant oxygen deficiency (Fig. 4c) arising from the low-temperature synthesis route. A DFT calculation by Jia *et al.* revealed that, the band gap of a N, S-codoped TiO_2 can be narrowed to be. 2.77 eV[44]. The further red-shift for the Au-decorated films was attributed mainly to the interaction of Au and TiO_2, which might introduce an intra-gap level inside the band gap of TiO_2[37]. Considering the relatively lower Au content for the Branched-Au-NW (0.36%) when compared with the Branched-NW-Au (0.51%), as determined by ICP-MS, both the higher light harvesting capability and the slightly lower band gap once again convinced the importance of the Au-location. A rough explanation for the enhanced LSPR arising from Au nanoparticles in Branched-Au-NW could be that the contacting surface area between Au and TiO_2 is higher than that in Branched-NW-Au.

Photocatalytic Activity. Photocatalytic activities of the three TiO_2 nanoforests were evaluated by decomposing rhodamine B in water under UV and visible light illuminations, respectively. In absence of any photocatalysts, about 95% and 97% dye molecules remained after 60 min of UV and visible light illuminations. The dark absorption capacity is enhanced after the Au-decoration, which can be ascribed to the interaction of Au and dye molecules. For comparison purpose, thin films of Degussa P25 TiO_2 nanoparticles (ca. 3.0 μm in thickness, refer to the literature[45] for the fabrication route), which are generally adopted as a benchmark, were also subjected to the photocatalytic activity evaluations under the identical conditions.

The $HAuCl_4$ concentrations adopted for the Au-decoration were firstly optimized (Supplementary Figure S2). It illustrates that, for both Au-decorated films, there is an optimum $HAuCl_4$ concentration (0.040 mM). It can thus be inferred that, certain amounts of Au nanoparticles introduced to the TiO_2 nanoforests enhanced the photocatalytic activity. However, excess Au nanoparticles aggregate to serve as recombination centers for photogenerated charges, leading to an inferior performance[46]. Figure 8a,b indicates the photodegradation curves, which can be fitted well assuming a pseudo-first-order kinetics[47],

$$ln\ \frac{c_0}{c} = kt$$

where c is the dye concentration after illumination for a duration t, c_0 is the dye concentration after the dark adsorption, and k is the pseudo-first-order reaction rate constant, which can be obtained by the slope of the straight lines through zero. Figure 8c,d shows the corresponding fitting results and Table 2 lists the reaction rate constants, which were derived using the average data obtained from three repetitive tests. Under the UV light illumination, the reaction rate constant increased from 0.86 to $2.5 \times 10^{-2}\,min^{-1}$ after the Au-decoration of the Branched-NW. Simply controlling the location of the Au nanoparticles to distribute mainly along the anatase/rutile phase junctions, the reaction rate constant further increased to $4.7 \times 10^{-2}\,min^{-1}$, which is nearly 5 times higher when compared with the Branched-NW specimen. The Au location affects also the photocatalytic activity under the visible light illumination.

Photocatalytic degradations of *p*-nitrophenol and phenol under the UV light illumination, in the presence of the various Au/TiO_2 films were also evaluated. Figure 9 and Table 2 show that, the same trend can be discerned.

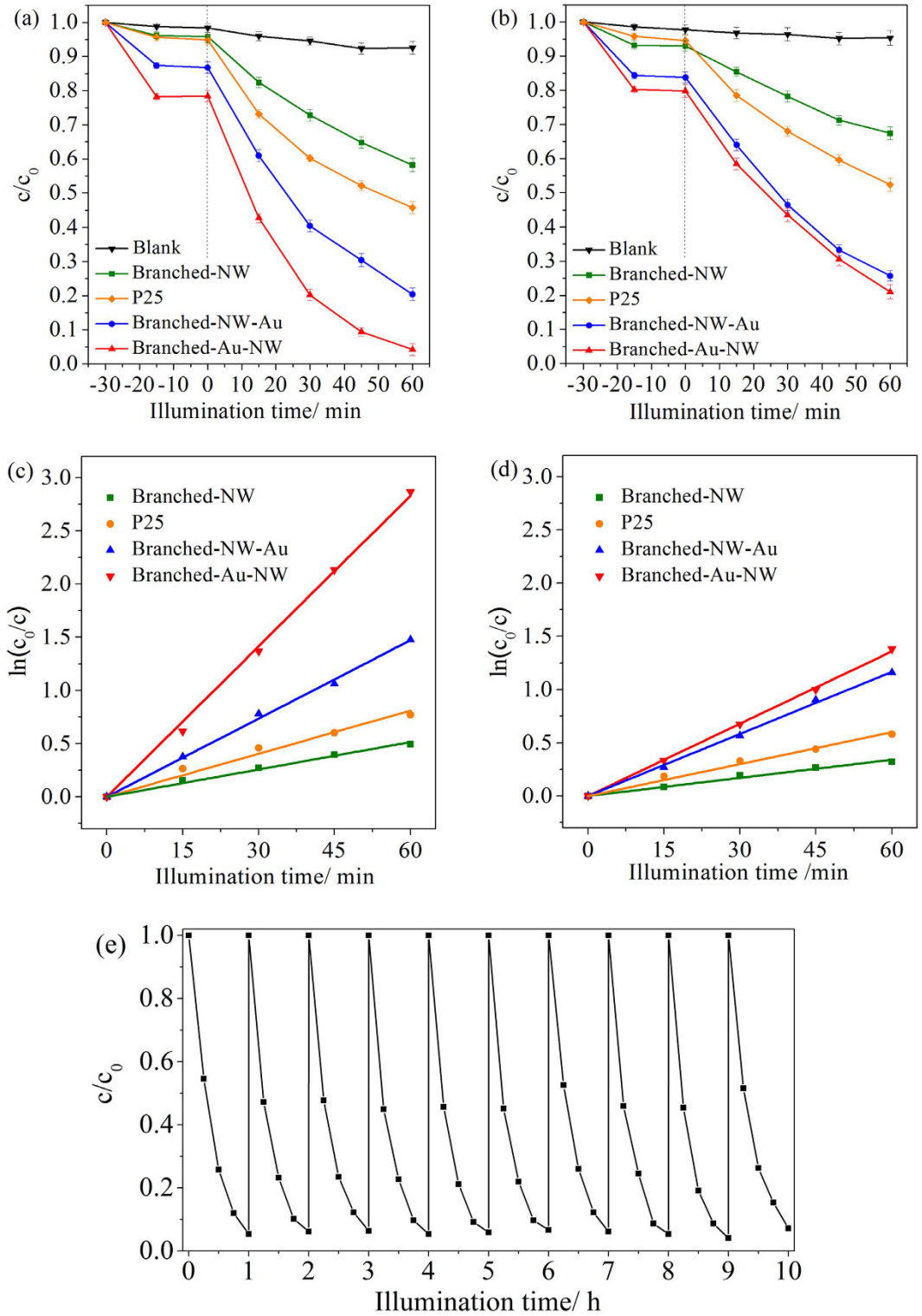

Figure 8. Photodegradation curves of rhodamine B in water in the presence of the P25, Branched-NW, Branched-NW-Au, and Branched-Au-NW, under (**a**) UV light, and (**b**) visible light illumination. (**c**,**d**) Represent the corresponding fitting results assuming a pseudo-first order reaction. The cycling performance of the Branched-Au-NW is illustrated in (**e**), under the UV light illumination.

Therefore, it can be concluded that, the photocatalytic activity of the branched TiO_2 film was enhanced after the Au decoration and the position of Au nanoparticles really has a great impact on the photocatalytic activity. Due to the insufficient efficiency of the present Au/TiO_2 films under the visible light illumination, the photocatalytic degradations of *p*-nitrophenol and phenol under visible light is not presented in the current investigation.

Films	P25	Branched-NW	Branched-NW-Au	Branched-Au-NW
UV + RhB	1.4	0.86	2.5	4.7
UV+ *p*-nitrophenol	/	0.11	0.16	0.22
UV+ phenol	/	0.07	0.11	0.17
Vis + RhB	1.0	0.57	1.9	2.3

Table 2. Reaction rate constants (k, $\times 10^{-2}\,min^{-1}$) for the different organics in the presence of various TiO_2 nanoforests and under the illumination of UV and visible light.

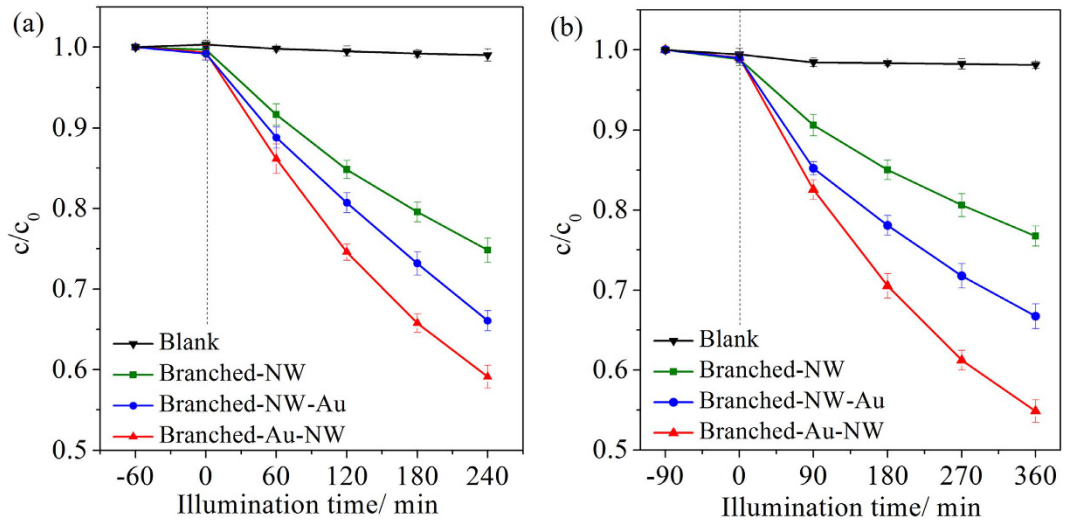

Figure 9. Photodegradation curves of (**a**) *p*-nitrophenol and (**b**) phenol under UV light illumination.

Photosensitive materials are argued to be not suitable as probe chemicals for photocatalytic activity tests, especially those for evaluation of activity under visible light[48]. Further study is thus demanded to disclose the effects of Au-locations on photodegradations of organics besides rhodamine B molecules.

The trapping experiment was employed to disclose the possible photocatalysis mechanism (Supplementary Figure S3). It is inferred that OH•, h^+, and $O_2\bullet^-$ all contribute to the photocatalytic reaction. The superoxide radicals $O_2\bullet^-$ are the major active species responsible for this photocatalytic oxidation reaction, followed by the photogenerated holes h^+, and the hydroxyl radical OH•.

Mechanism. Figure 10 provides a possible explanation for the beneficial effects arising from Au nanoparticles located between the anatase/rutile phase junctions in the present 1D branched TiO_2 nanowires. Because Supplementary Figure S3 indicates that superoxide radicals $O_2\bullet^-$ contribute the most to the photocatalytic reaction; only the degradation route via $O_2\bullet^-$ is presented in Fig. 10. It is well established that anatase/rutile phase junction effectively suppresses the recombination of photogenerated electron-hole pairs[30,49–51]; however, the exact charge transfer direction still remains a controversy[25,52]. Herein, the energetic alignment of the band edges of the anatase and rutile polymorphs of TiO_2 suggested recently by Scanlon *et al.* is adopted[52].

UV Light Illumination. As illustrated in Fig. 10a, under UV light irradiation, photogenerated electrons transfer from rutile to anatase, which results in an enhanced charge separation rate and hence improved photocatalytic activity. In addition, it has been proved that O_2 reduction by the photo-induced electrons on the rutile surface is inefficient because of the low affinity between the surface and O_2. In contrast, anatase is more active for O_2 reduction[13]. As a result, the electron transfer from rutile to anatase accelerates the photodegradation procedure, especially for which superoxide radicals $O_2\bullet^-$ play the key role (Supplementary Figure S3).

In case that the TiO_2 nanoforests were subjected to a final Au-decoration (Branched-NW-Au), Au nanoparticles prefer to locate on rutile surfaces (Fig. 5c,d). Because of the Shottky barrier between Au and TiO_2 semiconductor, the photoexcited electrons from rutile will also transfer to Au nanoparticles[13,14], except for the migration to anatase. Thus, Au nanoparticles act as the electrons accepting species at the Au/rutile interface, suppressing further the recombination of photogenerated charges (Fig. 10c). The reaction rate constant thus increased from 0.86 to $2.5 \times 10^{-2}\,min^{-1}$ (UV + RhB, Table 2). When Au nanoparticles are loaded on the interface between anatase and rutile in the TiO_2 nanoforests, as for the Branched-Au-NW, they provide a path for rapid and effective electron migrations from rutile to anatase[53], which significantly enhances the positive effects arising from the anatase/rutile phase junction (Fig. 10e). Such a function is more effective for the charge separation, contributing to an even higher reaction rate constant of $4.7 \times 10^{-2}\,min^{-1}$ (UV + RhB, Table 2). The enhanced charge separation is supported by the PL measurement (Fig. 6).

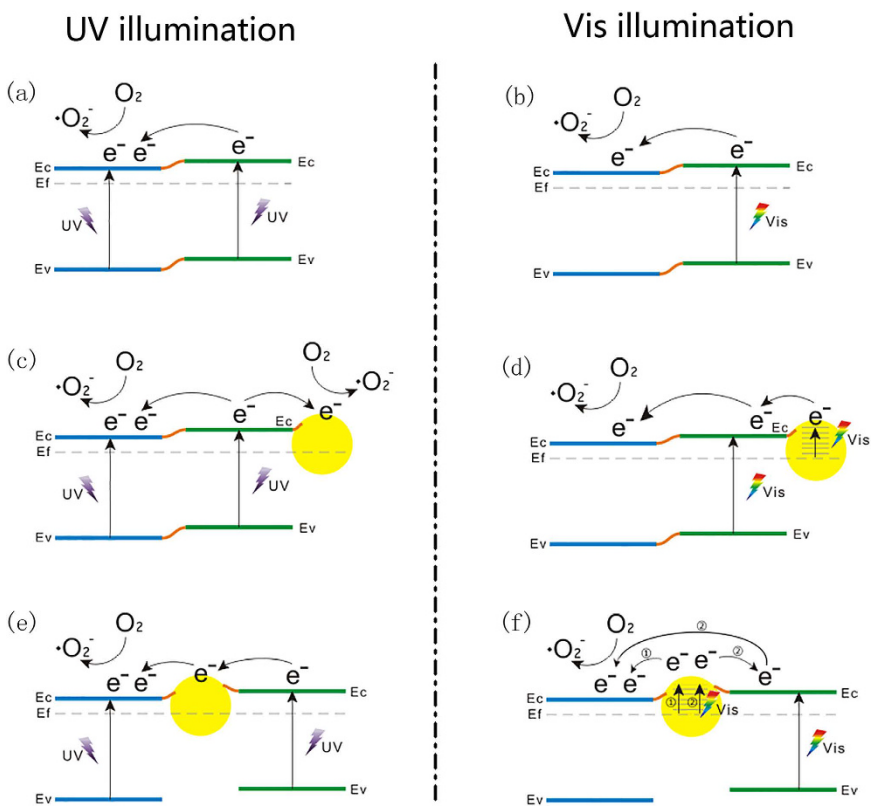

Figure 10. Schematic images showing the enhanced photocatalytic efficiency arising from the intermediate Au-loading for the TiO_2 nanoforests under the illumination of (**a**,**c**,**e**) UV and (**b**,**d**,**f**) visible light: (**a**,**b**) Branched-NW; (**c**,**d**) Branched-NW-Au; (**e**,**f**) Branched-Au-NW. For simplicity, the degradation route *via* photogenerated holes h^+ and hydroxyl radicals OH• is not shown.

Visible Light Illumination. In the current investigation, the Branched-NW possessed a band gap of 2.80 eV, which corresponds to a wavelength of ca. 440 nm (Fig. 7); therefore, under the illumination of visible light (>420 nm), it is possible for the rutile branch to absorb the photons with appropriate energy to initiate the photocatalytic reaction (Fig. 10b). The additional electrons arising from the LSPR effect of Au nanoparticles, which may also transfer to anatase to initiate the photodegradation reaction there (Fig. 10d), explains the increased reaction rate constant from $0.57 \times 10^{-2}\,min^{-1}$ for Branched-NW to $1.9 \times 10^{-2}\,min^{-1}$ for Branched-NW-Au (Vis + RhB, Table 2). The further enhanced reaction rate constant for Branched-Au-NW ($2.3 \times 10^{-2}\,min^{-1}$) is in good accordance with Tsukamoto *et al.*[13]. Here, Au nanoparticles locate preferably at the interface of anatase/rutile, upon the visible light illumination, the LSPR induced electrons transfer from Au nanoparticles to the tightly bound rutile and then through the phase junction to well-conjugated anatase, where the electrons react with surface adsorbed O_2 to form $O_2\bullet^-$ to assist photodegradations of rhodamine B in water (Path 2, Fig. 10f)[13,14]. Because Au nanoparticles contact with both anatase and rutile (Fig. 2d), we believe that, photogenerated electrons arising from the LSPR effect may also transfer directly to the adjacent anatase, which additionally contribute to the enhanced photocatalytic activity (Path 1, Fig. 10f).

Cycling Performance and mineralization capability. Long-term stability is a major concern of photocatalysts. Figure 8e shows the cycling performance of the Branched-Au-NW film. For up to 10 cycles, no remarkable decay can be discerned, which evidenced the excellent stability of the present Au-decorated TiO_2 nanoforests. The present Branched-Au-NW film is also capable of inducing deep mineralization of organics in water after UV illumination for certain durations. A total organic carbon (TOC) reduction of ca. 64.2% was achieved for the rhodamine B solution after the UV light illumination for 1 h when assisted by the Branched-Au-NW film. The liquid chromatography (LC) spectra (Supplementary Figure S4), which were utilized to determine the phenol's concentration during the photodegradation procedure under the UV illumination, shows that, although the P25 film has a higher efficiency on photodegradations of phenol, less by-products can be discerned for the Au/TiO_2 photocatalyst (Branched-Au-NW). This further supports the capability of the present Au/TiO_2 photocatalyst to achieve a deep mineralization of organics in water.

Conclusion

Titania nanoforests, which consisted of anatase nanowires surrounded by radially grown rutile branches, were synthesized on metallic Ti substrates through multi-steps of H_2O_2 oxidation, intermediate calcination, and sulfuric acid treatment. A photo-reduction technique was then applied to decorate Au nanoparticles. Altering the

order in the fabrication step is effective in controlling the preferred location of Au nanoparticles. Under the UV light illumination, Au nanoparticles, which located preferably at the interface of anatase/rutile, magnify the beneficial effects arising from the anatase/rutile phase junctions; whilst under the visible light illumination, the LSPR effect followed by the consecutive electron transfer results in improved photocatalysis. This finding evidenced the feasibility to further improve photocatalytic activity of multiple-phases semiconductor arrays with one-dimensional nanostructures through carefully controlling the location of noble metals.

Methods

Synthesis of TiO_2 Nanoforests. Figure 1 demonstrates schematically the three steps in sequence to synthesize TiO_2 nanoforests (abbreviated as **Branched-NW** hereafter) on metallic Ti substrates, that is, H_2O_2 oxidation, intermediate calcination, and H_2SO_4 treatment[34]. In a typical synthesis, each cleaned Ti plate ($5 \times 5 \times 0.01\ cm^3$ in size) was immersed in 50 mL of 8.8 M H_2O_2 solution containing 16 mM melamine ($C_3H_6N_6$) and 29 mM HNO_3, which was maintained at 80 °C for 48 h to grow hydrogen titanate ($H_2Ti_5O_{11}$) nanowire array on the surface. The Ti plate was then taken out, rinsed in sequence with ethanol and deionized water, and subjected to an intermediate thermal treatment in air at 260 °C for 1 h to decompose $H_2Ti_5O_{11}$ to amorphous TiO_2 embedded with poorly crystallized anatase. The Branched-NW was achieved by a final treatment in 50 mL of 5 mM H_2SO_4 aqueous solution at 80 °C for 48 h, which induced the formations of rutile TiO_2 branches that grow radially around the poorly crystallized anatase TiO_2 trunk[34].

Decoration of Au Nanoparticles at Controlled Locations. Au nanoparticles were decorated on Branched-NW via a photo-reduction method[54]. 0.44 mg of $HAuCl_4$ (corresponding to an initial concentration of ca. 0.040 mM), methanol (0.2 mL), and deionized water (34 mL) were mixed in a beaker. Branched-NW was immersed into the solution, which was bubbled with pure nitrogen gas, and then subject to the UV light (5.0 mW/cm^2) irradiation for 5 min. The specimens were dried at 80 °C in an oven overnight, which were designated as **Branched-NW-Au** hereafter. To vary the location of the Au nanoparticles, in a parallel experiment, the order in Au-deposition and H_2SO_4 treatment was exchanged. The specimens were noted as **Branched-Au-NW**.

Characterizations. Surface morphology of thin films was observed using a field emission scanning electron microscopy (FESEM, Hitachi S-4800) and a transmission electron microscopy (TEM, FEI, Tecnai G2 F20 S-TWIN, with EDS capabilities). To prepare the samples for TEM characterizations, the TiO_2 nanoforests were detached off from the Ti plate and then placed on a carbon pre-coated copper grid. The X-ray diffraction (XRD) tests were conducted on a Rigaku D/max-3B diffractmeter with Cu Kα radiation ($\lambda = 0.154056$ nm), operated at 40 kV, 36 mA. Raman spectra were collected using an Almega dispersive Raman system (Nicolet) and a Nd:YAG intracavity doubled laser operating at 532 nm with an incident power of 10 mW. The atomic ratio of Au and Ti was measured with inductively coupled plasma mass spectrometry (ICP-MS, XSeries II, Thermo Fisher Scientific, USA). For the ICP-MS measurement, the Au-decorated TiO_2 nanoforests were scratched off and dissolved in aqua regia. The X-ray photoelectron spectroscopy (XPS) spectra were collected using an ESCA spectrometer (S-Probe ESCA SSX-100S, Fisons Instrument) and monochromatized Al Kα X-ray (1486.8 eV) irradiation. The binding energy was normalized to the C 1 s energy (284.6 eV) for adventitious hydrocarbons as the indirect standard. The UV-Vis diffuse reflectance spectra were measured using a UV-Vis near-infrared spectrometer (UV-3150, Shimadzu). The ambient photoluminescence (PL) emission spectra characterizations were carried out on a fluorescence spectrophotometer (HITACHI F-4500) with an excited wavelength of 360 nm.

Photocatalytic Activity Evaluations. Titania thin films ($2.5 \times 2.5\ cm^2$ in size) were used to assist photocatalytic degradations of rhodamine B, *p*-nitrophenol and phenol in water (25 mL) in a Pyrex reactor with a water jacket, which is illustrated schematically in Supplementary Figure S5. Three repetitive tests were conducted to give the average value and error bar (standard deviation) as illustrated in the corresponding degradation curves. The initial concentration of rhodamine B is 0.005 mmol/L, while the initial concentrations of *p*-nitrophenol and phenol are 5 ppm and 10 ppm, respectively. The UV irradiation was provided by an 18 W UV lamp and the visible light by a 500 W Xe-lamp with a 420 nm UV-cut filter. The UV and visible light intensity reaching the sample was measured to be ca. 5.0 mW/cm^2 and 200.0 mW/cm^2, respectively, using irradiance meters (model: UV-A and FZ-A, Beijing Normal university, China, measured for the wavelength of 365 nm for UV light and 400–1000 nm for the visible light). The solution was stirred and exposed to air during the photocatalytic reaction. The change in the rhodamine B and *p*-nitrophenol concentrations was monitored with a UV-Vis spectrophotometer (UV-1800PC, Shanghai Mapada, Shanghai, China) at a wavelength of 553 nm and 317 nm, respectively. The phenol concentration was analyzed by liquid chromatography on a Wufeng LC100 (WondaCract C18-ODS column, and 50% CH_3OH aqueous solution as an eluent). The total organic carbon (TOC) of rhodamine B was measured with a Total Organic Carbon Analyzer (Multi N/C 3100).

To investigate the effects of the active species generated during the photocatalytic reaction under the UV illumination and in the presence of the Branched-Au-NW, the free radicals capture experiments were conducted[55]. The three major oxidants involved in photodegradations of organics in water, that is, hydroxyl radical (OH•), hole (h^+), and superoxide radical ($O_2^{\bullet -}$), were trapped by adding 0.5 mL of tert-butanol (t-BuOH), 0.1 mM of ammonium oxalate (AO), and 0.5 mM of 1, 4-benzoquinone (BQ), respectively, into the rhodamine B solutions.

References

1. Chen, X. & Mao, S. S. Titanium Dioxide Nanomaterials: Synthesis, Properties, Modifications, and Applications. *Chem. Rev.* **107,** 2891–2959 (2007).
2. Moniz, S. J. A., Shevlin, S. A. & Martin, D. J. Visible-Light Driven Heterojunction Photocatalysts for Water Splitting–A Critical Review. *Energ. Environ. Sci.* **8,** 731–759 (2015).

3. Xiang, Q., Cheng, B. & Yu, J. Graphene-Based Photocatalysts for Solar-Fuel Generation. *Angew. Chem. Int. Ed.* **54,** 11350–11366 (2015).
4. Ghosh, S., Kouamé, N. A. & Ramos, L. Conducting Polymer Nanostructures for Photocatalysis under Visible Light. *Nat. mater.* **14,** 505–511 (2015).
5. Bridewell, V. L., Alam, R. & Karwacki, C. J. CdSe/CdS Nanorod Photocatalysts: Tuning the Interfacial Charge Transfer Process through Shell Length. *Chem. Mater.* **27,** 5064–5071 (2015).
6. Fujishima, A. & Honda, K. Electrochemical Photolysis of Water at A Semiconductor Electrode. *Nature* **238,** 37–38 (1972).
7. Banerjee, B., Amoli, V. & Maurya, A. Green Synthesis of Pt-Doped TiO_2 Nanocrystals with Exposed (001) Facets and Mesoscopic Void Space for Photo-Splitting of Water under Solar Irradiation. *Nanoscale* **7,** 10504–10512 (2015).
8. Choi, Y., Kim, H. & Moon, G. Boosting up the Low Catalytic Activity of Silver for H_2 Production on Ag/TiO_2 Photocatalyst: Thiocyanate as A Selective Modifier. *ACS Catal.* **6,** 821–828 (2016).
9. Fujiwara, K., Müller, U. & Pratsinis, S. E. Pd Subnano-Clusters on TiO_2 for Solar-Light Removal of NO. *ACS Catal*. **3,** 1887–1893 (2016)
10. Zhang, D. Q. *et al.* Au Nanoparticles Enhanced Rutile TiO_2 Nanorod Bundles with High Visible-Light Photocatalytic Performance for NO Oxidation. *Appl. Catal. B-Environ.* **147,** 610–616 (2014).
11. Nalbandian, M. J. *et al.* Tailored Synthesis of Photoactive TiO_2 Nanofibers and Au/TiO_2 Nanofiber Composites: Structure and Reactivity Optimization for Water Treatment Applications. *Environ. Sci. Technol.* **49,** 1654–1663 (2015).
12. McEntee, M., Stevanovic, A., Tang, W. J., Neurock, M. & Yates, J. T. Electric Field Changes on Au Nanoparticles on Semiconductor Supports-the Molecular Voltmeter and Other Methods to Observe Adsorbate-Induced Charge-Transfer Effects in Au/TiO_2 Nanocatalysts. *J. Am. Chem. Soc.* **137,** 1972–1982 (2015).
13. Tsukamoto, D. *et al.* Gold Nanoparticles Located at the Interface of Anatase/Rutile TiO_2 Particles as Active Plasmonic Photocatalysts for Aerobic Oxidation. *J. Am. Chem. Soc.* **134,** 6309–6315 (2012).
14. Wen, Y., Liu, B. T., Zeng, W. & Wang, Y. H. Plasmonic Photocatalysis Properties of Au Nanoparticles Precipitated Anatase/Rutile Mixed TiO_2 Nanotubes. *Nanoscale* **5,** 9739–9746 (2013).
15. Cheng, H., Fuku, K. & Kuwahara, Y. Harnessing Single-Active Plasmonic Nanostructures for Enhanced Photocatalysis under Visible Light. *J. Mater. Chem. A* **3,** 5244–5258 (2015).
16. Ma, L. *et al.* Synthesis of Dumbbell-Like Gold-Metal Sulfide Core-Shell Nanorods with Largely Enhanced Transverse Plasmon Resonance in Visible Region and Efficiently Improved Photocatalytic Activity. *Adv. Funct. Mater.* **25,** 898–904 (2015).
17. Zielinska-Jurek, A. *et al.* Preparation and Characterization of Monometallic (Au) and Bimetallic (Ag/Au) Modified-Titania Photocatalysts Activated by Visible Light. *Appl. Catal. B-Environ.* **101,** 504–514 (2011).
18. Kimura, K., Naya, S. & Jin-nouchi, Y. TiO_2 Crystal Form-Dependence of the Au/TiO_2 Plasmon Photocatalyst's Activity. *J. Phys. Chem. C* **116,** 7111–7117 (2012).
19. Murdoch, M., Waterhouse, G. I. N. & Nadeem, M. A. The Effect of Gold Loading and Particle Size on Photocatalytic Hydrogen Production from Ethanol over Au/TiO_2 Nanoparticles. *Nat. Chem.* **3,** 489–492 (2011).
20. Tanaka, A., Sakaguchi, S. & Hashimoto, K. Preparation of Au/TiO_2 with Metal Cocatalysts Exhibiting Strong Surface Plasmon Resonance Effective for Photoinduced Hydrogen Formation under Irradiation of Visible Light. *ACS Catal.* **3,** 79–85 (2012).
21. Bian, Z., Tachikawa, T. & Zhang, P. Au/TiO_2 Superstructure-Based Plasmonic Photocatalysts Exhibiting Efficient Charge Separation and Unprecedented Activity. *J. Am. Chem. Soc.* **136,** 458–465 (2013).
22. Priebe, J. B., Radnik, J. & Lennox, A. J J. Solar Hydrogen Production by Plasmonic Au–TiO_2 Catalysts: Impact of Synthesis Protocol and TiO_2 Phase on Charge Transfer Efficiency and H_2 Evolution Rates. *ACS Catal.* **5,** 2137–2148 (2015).
23. Li, H., Zhou, Y. & Tu, W. State-of-the-Art Progress in Diverse Heterostructured Photocatalysts toward Promoting Photocatalytic Performance. *Adv. Funct. Mater.* **25,** 998–1013 (2015).
24. Kafizas, A., Wang, X. & Pendlebury, S. R. Where Do Photo-Generated Holes Go in Anatase: Rutile TiO_2? A Transient Absorption Spectroscopy Study of Charge Transfer and Lifetime. *J. Phys.Chem. A* **120,** 715–723 (2016).
25. Zhao, W. N., Zhu, S. C. & Li, Y. F. Three-Phase Junction for Modulating Electron–Hole Migration in Anatase–Rutile Photocatalysts. *Chem. Sci*. **6,** 3483–3494 (2015).
26. Sun, X., Dai, W. & Wu, G. Evidence of Rutile-to-Anatase Photo-Induced Electron Transfer in Mixed-Phase TiO_2 by Solid-State NMR Spectroscopy. *Chem. Commun.* **51,** 13779–13782 (2015).
27. Zhang, Y., Pei, Q. & Liang, J. Mesoporous TiO_2-Based Photoanode Sensitized by BiOI and Investigation of Its Photovoltaic Behavior. *Langmuir* **31,** 10279–10284 (2015).
28. Han, C., Wang, Y. & Lei, Y. *In Situ* Synthesis of Graphitic-C_3N_4 Nanosheet Hybridized N-Doped TiO_2 Nanofibers for Efficient Photocatalytic H_2 Production and Degradation. *Nano Res*. **8,** 1199–1209 (2015).
29. Liu, L., Yang, W. & Sun, W. Creation of Cu_2O@ TiO_2 Composite Photocatalysts with p–n Heterojunctions Formed on Exposed Cu_2O Facets, Their Energy Band Alignment Study, and Their Enhanced Photocatalytic Activity under Illumination with Visible Light. *ACS Appl. Mater. Inter.* 7, 1465–1476 (2015).
30. Ge. M. *et al.* A Review of One-Dimensional TiO_2 Nanostructured Materials for Environmental and Energy Applications. *J. Mater. Chem. A* **4,** 6772–6801 (2016).
31. Sheng, X., He, D., Yang, J., Zhu, K. & Feng, X. Oriented Assembled TiO_2 Hierarchical Nanowire Arrays with Fast Electron Transport Properties. *Nano Lett.* **14,** 1848–1852 (2014).
32. Wu, W. Q., Xu, Y. F., Rao, H. S., Su, C. Y. & Kuang, D. B. Multistack Integration of Three-Dimensional Hyperbranched Anatase Titania Architectures for High-Efficiency Dye-Sensitized Solar Cells. *J. Am. Chem. Soc.* **136,** 6437–6445 (2014).
33. Liu, C., Tang, J., Chen, H. M., Liu, B. & Yang, P. A Fully Integrated Nanosystem of Semiconductor Nanowires for Direct Solar Water Splitting. *Nano Lett.* **13,** 2989–2992 (2013).
34. Wu, J. M. & Yin, J. X. A Facile Solution-Based Approach to A Photocatalytic Active Branched One-Dimensional TiO_2 Array. *RSC Adv*. **5,** 3465–3469 (2015).
35. Sun, J. & Wu, J. M. A Comparative Study on Photocatalytic Activity of Titania Nanowires Subjected to High-Temperature Calcination and Low-Temperature HCl Treatment. *Sc. Adv. Mater.* **5,** 549–556 (2013).
36. Sun, J., Wen, W. & Wu, J. M. Low-Temperature Transformation of Titania Thin Films from Amorphous Nanowires to Crystallized Nanoflowers for Heterogeneous Photocatalysis. *J. Am. Ceram. Soc.* **96,** 2109–2116 (2013).
37. Zhu, Y. F. *et al.* Fabrication and Photoelectrochemical Properties of ZnS/Au/TiO_2 Nanotube Array Films. *Phys. Chem. Chem. Phys.* **15,** 4041–4048 (2013).
38. Su, F. L. *et al.* Dendritic Au/TiO_2 Nanorod Arrays for Visible-Light Driven Photoelectrochemical Water Splitting. *Nanoscale* **5,** 9001–9009 (2013).
39. Li, D. Z. *et al.* New Synthesis of Excellent Visible-Light $TiO_{2-x}N_x$ Photocatalyst Using a Very Simple Method. *J. Solid State Chem.* **180,** 2630–2634 (2007).
40. Lai, L. L. & Wu, J. M. A Facile Solution Approach to W, N Co-Doped TiO_2 Nanobelt Thin Films with High Photocatalytic Activity. *J. Mater. Chem. A* **3,** 15863–15868 (2015).
41. Zhang, X. M., Chen, Y. L., Liu, R. S. & Tsai, D. P. Plasmonic Photocatalysis. *Rep. Prog. Phys.* **76,** 4 (2013).
42. Zhang, X., Liu, Y. & Kang, Z. H. 3D Branched ZnO Nanowire Arrays Decorated with Plasmonic Au Nanoparticles for High-Performance Photoelectrochemical Water Splitting. *ACS Appl. Mat. Inter.* **6,** 4480–4489 (2014).

43. Sanchez, E. & Lopez, T. Effect of the Preparation Method on the Band Gap of Titania and Platinum-Titania Sol-Gel Materials. *Mater. Lett.* **25,** 271–275 (1995).
44. Jia, L. C. *et al.* Enhanced Visible-Light Photocatalytic Activity of Anatase TiO_2 through N and S Codoping. *Appl. Phys. Lett.* **98,** 211903 (2011).
45. Wu, J. M., Zhang, T. W. & Zeng, Y. W. Large-Scale Preparation of Ordered Titania Nanorods with Enhanced Photocatalytic Activity. *Langmuir* **21,** 6995–7002 (2005).
46. Li, H. X. *et al.* Mesoporous Au/TiO_2 Nanocomposites with Enhanced Photocatalytic Activity. *J. Am. Chem. Soc.* **129,** 4538–4539 (2007).
47. Wu, J. M. & Zhang, T. W. Photodegradation of Rhodamine B in Water Assisted by Titania Films Prepared through A Novel Procedure. *J. Photochem. Photobiol. A-Chem.* **162,** 171–177 (2004).
48. Yan, X. L., Ohno, T., Nishijima, K., Abe, R. & Ohtani, B. Is Methylene Blue an Appropriate Substrate for a Photocatalytic Activity Test? A Study with Visible-Light Responsive Titania. *Chem. Phys. Lett.* **429,** 606–610 (2006).
49. Zhang, J., Xu, Q., Feng, Z., Li, M. & Li, C. Importance of the Relationship between Surface Phases and Photocatalytic Activity of TiO_2. *Angew. Chem. Int. Ed.* **47,** 1766–1769 (2008).
50. Xu, Q. *et al.* Enhancing Hydrogen Production Activity and Suppressing CO Formation from Photocatalytic Biomass Reforming on Pt/TiO_2 by Optimizing Anatase-Rutile Phase Structure. *J. Catal.* **278,** 329–335 (2011).
51. Hurum, D. C., Agrios, G. A. & Gary, A. Kimberly Explaining the Enhanced Photocatalytic Activity of Degussa P25 Mixed-Phase TiO_2 Using EPR. *J. Phys. Chem. B* **107,** 4545–4549 (2003).
52. Scanlon, D. O. *et al.* Band Alignment of Rutile and Anatase TiO_2. *Nat. Mater.* **12,** 798–801 (2013).
53. Li, J. T. *et al.* Solar Hydrogen Generation by a CdS-Au-TiO_2 Sandwich Nanorod Array Enhanced with Au Nanoparticle as Electron Relay and Plasmonic Photosensitizer. *J. Am. Chem. Soc.* **136,** 8438–8449 (2014).
54. Zheng, Z. K. *et al.* Facile *in situ* Synthesis of Visible-Light Plasmonic Photocatalysts M@TiO_2 (M = Au, Pt, Ag) and Evaluation of Their Photocatalytic Oxidation of Benzene to Phenol. *J. Mater. Chem.* **21,** 9079–9087 (2011).
55. Jiang, Z. F., Zhu, C. Z., Wan, W. M., Qian, K. & Xie, J. M. Constructing Graphite-Like Carbon Nitride Modified Hierarchical Yolk–Shell TiO_2 Spheres for Water Pollution Treatment and Hydrogen Production. *J. Mater. Chem. A* **4,** 1806–1818 (2016).

Acknowledgements

We gratefully acknowledge financial support for this work from Department of Science Technology of Zhejiang Province (No. 2015C31034) and National Natural Science Foundation of China (No. 51502065).

Author Contributions

J.M.W. and W.W. conceived the concept and experiments. Y.Y. and X.Y.Q. carried out the materials synthesis and characterizations. J.B.L. carried out the TEM analysis. Y.Y. and J.M.W. co-wrote the paper. All authors discussed the results and commented on the manuscript.

Additional Information

Supplementary information accompanies this paper at http://www.nature.com/srep

Competing financial interests: The authors declare no competing financial interests.

How to cite this article: Yu, Y. *et al.* UV and visible light photocatalytic activity of Au/TiO_2 nanoforests with Anatase/Rutile phase junctions and controlled Au locations. *Sci. Rep.* **7**, 41253; doi: 10.1038/srep41253 (2017).

Publisher's note: Springer Nature remains neutral with regard to jurisdictional claims in published maps and institutional affiliations.